ACS APPLIED ENERGY MATERIALS

www.acsaem.org Article

Intense Pulse Light Annealing of Perovskite Photovoltaics Using Gradient Flashes

Amir H. Ghahremani, Sahar Pishgar, Jitendra Bahadur, and Thad Druffel*

Cite This: *ACS Appl. Energy Mater.* 2020, 3, 11641−11654 Read Online

ACCESS | Metrics & More | Article Recommendations | Supporting Information

ABSTRACT: Perovskite solar cells (PSCs) have been fabricated through high-speed and low-cost depositions but often require long annealing. Intense pulse light (IPL) can anneal thin films in seconds after deposition by inducing very high temperatures lasting for milliseconds, and multiple flashes can be used to tune the temperature profile. In this study, a gradient flash annealing (GFA) approach is introduced and compared to uniform flash annealing (UFA) by investigating the crystallinity, morphology, and phase evolution of the $CH_3NH_3PbI_3$ perovskite films and their impact on PSC performance. Unlike UFA, low-intensity pulsed irradiation during the pre-annealing stage of GFA played a significant role on enhancing the PSC performance by forming pure-phase $CH_3NH_3PbI_3$ perovskite thin films with superior morphology and high crystallinity. To understand the kinetics, a transient thermal simulation using ANSYS was developed and confirmed with an experimental setup. The results combined with microscopy and spectrophotometry were used to visualize how duration, delay time, photon flux, and flash count parameters participated in crystallization, phase, and morphology evolution. The IPL annealing induced rapid surface temperature increase, reaching as high as 800 °C, while produced well-developed and bound perovskite grains without any surface defects in an uncontrolled ambient environment with high humidity (>60%). The study resulted in PSCs with maximum efficiency and fill factor of 9.27 and 69.92% for the UFA and 11.75 and 68% when annealed through the GFA approach, respectively. This work utilized IPL as the sole thermal source for post-deposition annealing to rapidly fabricate efficient PSCs in only 10 s, which opens the pathway for high-speed, low-cost, and large-scale automated fabrication of perovskite photovoltaics and semiconductors.

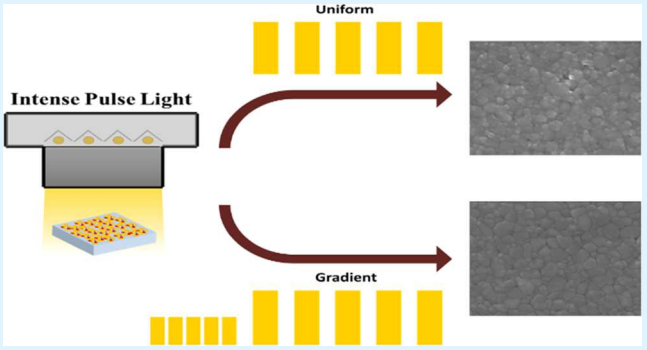

KEYWORDS: *IPL, UFA, GFA, IPL temperature measurement, transient thermal simulation, perovskite solar cell*

1. INTRODUCTION

Over the past few years, considerable research and development has made organic−inorganic perovskite solar cells (PSCs) a viable technology with the possibility of large-scale and high-throughput production through cost-effective manufacturing. Selection of potential materials as well as the optimization of precursor chemistries and fabrication procedures has aided achieving superior thin films from materials possessing high charge carrier mobility,[1] suitable band gap,[2] defect tolerance,[3,4] low exciton binding energy,[5] long charge carrier diffusion length, and high optical absorption.[6] These achievements have increased the efficiency of PSCs to over 25%,[7] thus taking a closer step to the Shockley−Queisser limit of 33%.[8] The conventional structure of PSCs includes a solution-processed light absorber film sandwiched between a p-type and an n-type charge carrier thin film,[9] in which the optimal processing conditions of individual films are necessary to obtain maximum device efficiency. The fabrication sequence includes substrate surface preparation, a thin film coating process, and a post-process annealing step to crystallize the material. The combination of these processes should yield optimum crystallization while enabling uniform films without discontinuities and defects. Providing optimum instrument parameters[10] as well as taking advantage of promising approaches such as sequential step coating and annealing,[11,12] antisolvents,[13] additives,[14] in situ heating of the as-deposited thin films,[15] and the use of special environments to fabricate the films[16] has shown to remarkably improve the charge carrier transport and efficiency of PSCs through enhanced film morphology and crystallization.

Post-process annealing is another factor that plays a significant role on thin film quality, overall performance, and manufacturing cost of photovoltaic modules.[17−19] The post-process annealing has been accomplished using ovens, furnaces, radiative heaters, and convective blowing. Despite

Received: June 29, 2020
Accepted: November 18, 2020
Published: December 2, 2020

https://dx.doi.org/10.1021/acsaem.0c01520
ACS Appl. Energy Mater. 2020, 3, 11641−11654

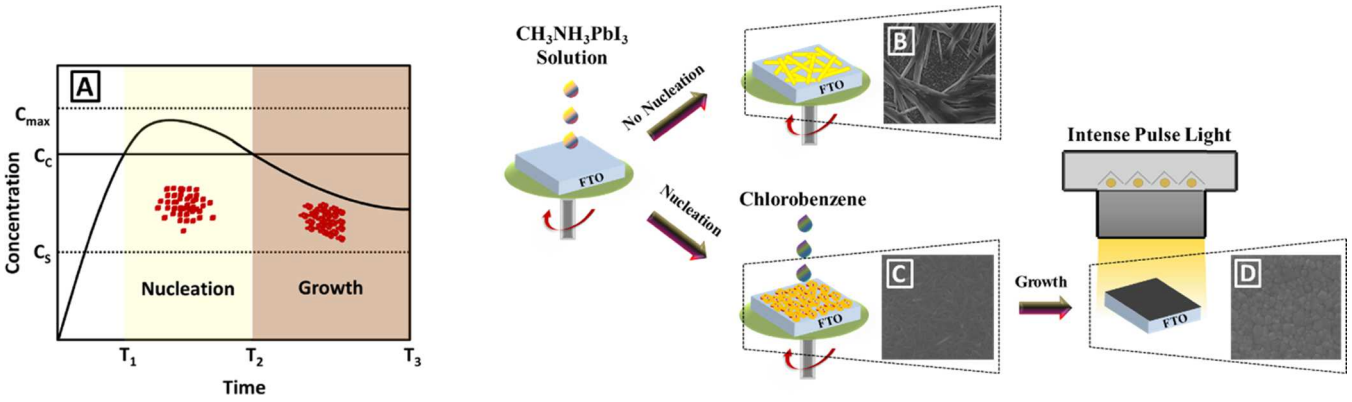

Figure 1. (A) LaMer curve; formation of (B) perovskite dendrites without antisolvent treatment and (C) perovskite intermediate upon antisolvent treatment; and (D) grain growth of the intermediate phase upon annealing.

the prevalent use of these methods to fabricate efficient thin film photovoltaics, they are not favorable for high-throughput industrial-scale manufacturing as the high energy consumption accompanied by the high-temperature and long-term annealing increases the overall production cost as well as the energy and cost payback time of the fabricated modules.[18,19] In addition, roll-to-roll favorable plastic substrates, such as poly(ethylene terephthalate) (PET) and poly(ethylene 2,6-naphthalate) (PEN), have very limited operational temperatures, which requires utilizing other methods such as photonic annealing.

To date, various photonic annealing methods have been utilized to fabricate efficient PSCs. For instance, Sanchez and colleagues took advantage of flash infrared annealing (FIR) to anneal a TiO_2 electron transport layer (ETL) in 10 min.[20] They also annealed the perovskite films through 1.6−1.7 ms flash exposure followed by a 10 s hold in the chamber to accomplish the annealing process and reported PSCs with over 19% efficiency.[20,21] Other studies have also utilized IR annealing to fabricate efficient PSCs in a short period.[22,23] You and co-workers[24] fabricated efficient PSCs surpassing 20% efficiency through laser annealing of the perovskite films using lasers irradiating three different wavelengths of 405, 450, and 660 nm at a speed of 25 mm/min and achieved the maximum performance at 450 nm wavelength. The intense pulse light (IPL) annealing also exerts irradiation in the visible region to anneal large-area films and can be simply integrated into high-speed manufacturing.

IPL is a rapid thermal technique, which has been used to cure, sinter, and anneal polymer, metallic, and semiconducting thin films.[25,26] IPL utilizes gas discharge lamps containing a noble gas, typically Xenon, that, when excited by a large potential, releases an extremely rapid flash of intense light in millisecond(s). Unlike IR, IPL irradiation has a broad spectrum from near UV to IR, which makes xenon lamps favorable for annealing of various semiconducting materials with different absorptivity. The energetic photons are absorbed by the semiconducting thin films and allow for instant crystallization of large-area semiconductor and photovoltaic thin film materials without imposing thermal degradation, which is compatible with roll-to-roll favorable plastic substrates.[27] The absorbed photothermal energy induces material phase evolution and grain growth, leading to a decreased grain boundary density, which enhances the quantity of extracted charge carriers. Therefore, optimum annealing is necessary to control the crystallization, minimize the series and shunt resistance pathways, and, thus, enable efficient PSCs.

IPL has been used to anneal the thin film materials without altering the chemical structure of the annealed composite[28−31] and has also been utilized to develop another chemical structure, resulting in thin films with different chemical properties upon annealing.[32−34] In both applications, applying optimum annealing parameters, including flash duration, interval time between flashes, flash count, and the applied energy per flash, is significant to obtain thin films with superior morphology, high phase purity, and crystallinity. Various studies have, so far, reported fabrication of efficient PSCs through IPL annealing of the charge carrier,[32] perovskite photoabsorber,[34−36] and back-contact electrode thin films.[37,38] In these studies, only one layer was annealed through IPL. In addition, a short-term or prolonged medium-to-high-temperature conductive pre-annealing step to evaporate the solvents and initiate phase change and crystallization has been utilized before IPL annealing;[29,39] yet, rapid fabrication of PSCs through IPL annealing of all of the semiconducting films has not been established. Therefore, it is necessary to develop new approaches spanning all of the IPL annealing parameters to enable rapid automated fabrication of efficient PSCs without the necessity for intermediate short-term or long-term conductive and convective annealing.

Successful fabrication of PSCs through IPL annealing of a spin-coated SnO_2 (ETL) and a perovskite photoabsorber was previously reported; however, the perovskite films required 30 s preheating to evaporate the solvents and initiate crystallization before IPL annealing.[35,40] In this paper, we report rapid fabrication of efficient planar PSCs with a glass/fluorine-doped tin oxide (FTO)/SnO_2/perovskite/Spiro-MeOTAD/Au architecture by directly annealing the spin-coated films through IPL without short- or long-term conductive annealing. The perovskite films were annealed entirely through IPL using a gradated approach which could form good morphology with high crystallinity. The study was conducted by characterizing the perovskite films through field emission scanning electron microscopy (FE-SEM), photoluminescence (PL), UV−vis spectrometry, X-ray diffraction (XRD), and voltammetry. In addition, an experimental setup and a two-dimensional (2D) ANSYS finite element analysis (FEA) were established to measure and model the maximum temperature at the surface of thin films, particularly the perovskite photoabsorber, during IPL annealing, respectively, and were then used to plot the Arrhenius plots explaining the enhanced PSC performance after gradient flash annealing (GFA).

https://dx.doi.org/10.1021/acsaem.0c01520
ACS Appl. Energy Mater. 2020, 3, 11641−11654

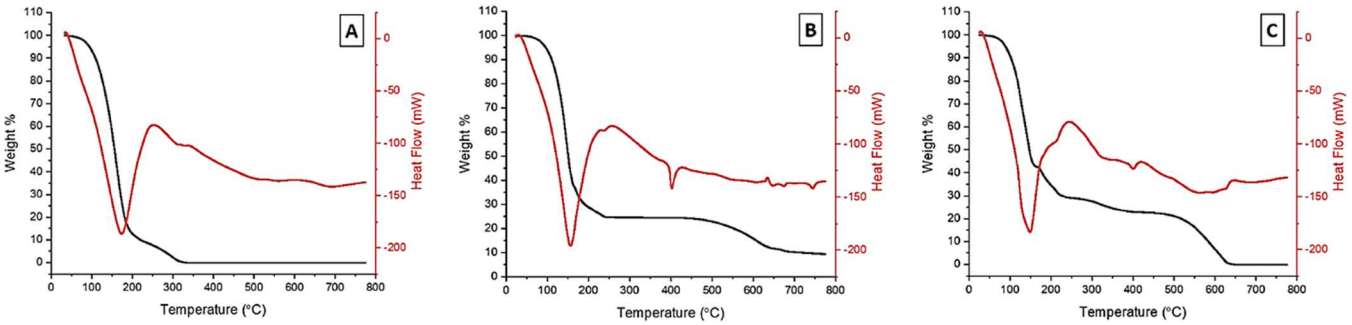

Figure 2. DSC−TGA curves for 1.4 M solutions of (A) CH_3NH_3I; (B) PbI_2; and (C) mixed $CH_3NH_3PbI_3$ perovskite precursor.

2. RESULTS AND DISCUSSION

Crystallization is a key factor to obtain efficient PSCs, and the applied annealing parameters should result in a highly crystalline perovskite pure black phase capable to produce charge carriers upon illumination. Perovskite photoabsorber crystallization includes nucleation of the as-deposited solution followed by grain growth that typically occurs during annealing. Nucleation kinetics of the perovskite film have been explained with the LaMer curve.[41,42] As shown in Figure 1A, the spinning process alters the fixed solubility, critical concentration, and maximum supersaturation limit of the room-temperature perovskite precursor through solvent evaporation, precipitating the solute after exceeding the maximum supersaturation level. At this stage, as shown in Figure 1B, the solute species agglomerate and form a rough opaque film with dense dendrite structures. Post-process annealing of this film would result in poor photovoltaic performance due to incomplete surface coverage and weak optical absorption. Therefore, a crystallization process through supersaturation of the precursor is necessary prior to annealing. In this process, chlorobenzene was dropped at the 10th second (T1) prior to the end of the spinning process. Upon spin-coating (T_3-T_1), a transparent film was obtained and, as shown in Figure 1C, numerous infinitesimal crystals arranged into smaller size dendrites were formed and covered the entire surface, which could indicate the formation of a $CH_3NH_3I{\cdot}PbI_2{\cdot}DMSO{\cdot}DMF{\cdot}CH_2I_2$ adduct and, thus, successful formation of a perovskite yellow intermediate.[43] This nucleation can be attributed to antisolvent dripping, which resulted in rapid stochastic intermolecular fluctuations of the atoms to form nuclei and, in turn, crystals, as well as the nuclei shear-off from the developing crystals to develop adjacent crystals and proliferate the nucleation throughout the surface,[44] thus consuming and decreasing the size of dendrite clusters. Subsequent annealing of the developed intermediate phase ($>T_3$) enables grain growth and formation of a perovskite black phase to produce charge carriers upon illumination (Figure 1D). Therefore, it is expected that the synergy of solvent extraction and solute diffusion would determine the phase purity, morphology, and PSC performance. Since the coating processes can take place in a short period, rapid fabrication of efficient PSCs is highly dependent on successful rapid annealing of the developed intermediate phase ($>T_3$). Therefore, taking advantage of adequate annealing approaches and applying optimum IPL annealing parameters are required to achieve maximum device performance.

To better understand how annealing would accomplish the perovskite film crystallization through phase change and crystal growth, thermogravimetry and differential scanning calorimetry (TGA−DSC) analysis of the CH_2I_2-assisted $CH_3NH_3PbI_3$ perovskite precursor and its constituents in the *N*,*N*-dimethylformamide (DMF)-dimethyl sulfoxide (DMSO)-CH_2I_2 solvent mixture was conducted up to 800 °C. Figure 2A shows the TGA−DSC curves for 1.4 M solution of CH_3NH_3I in the solvent mixture. The abrupt 80% weight loss in the TGA graph as well as the intense DSC endothermic peak at 174 °C is indicative of complete solvent evaporation. Right after this stage, the DSC curve indicates a strong exothermic peak with the maximum at 254 °C, determining maximized crystallization of CH_3NH_3I, while the TGA curve indicates a mild slope up to 330 °C where 100% mass loss is observed. This indicates that the CH_3NH_3I phases could remain in the film up to 254 °C and then sublimate from the perovskite film at higher temperatures and is consistent with other reports.[45] Similarly, as shown in Figure 2B, the DSC−TGA curve of the 1.4 M PbI_2 solution indicates two endothermic peaks at 157 and 402 °C, indicating complete solvent evaporation and melting of PbI_2, respectively. The high melting point indicates viability of PbI_2 up to this temperature, and further descend of the TGA graph for temperatures higher than 430 °C demonstrates PbI_2 decomposition and evaporation of the iodine phase as a result of Pb−I cleavage. Therefore, it can be inferred that the formation of crystal defects caused by CH_3NH_3I phase evaporation during annealing can be the potential factor for PSC performance degradation and instability which needs to be considered during IPL annealing and is consistent with other reports.[46,47] Compared to CH_3NH_3I, the DSC−TGA curves indicate a slightly lower volatile evaporation temperature in the case of PbI_2 solution, which indicates stronger intermolecular forces between the solvent mixture and CH_3NH_3I and a potential retarding factor for perovskite crystallization and is consistent with other reports.[48,49] Figure 2C indicates DSC−TGA curves of the CH_2I_2-assisted $CH_3NH_3PbI_3$ precursor, indicating complete solvent evaporation at 150 °C. The solvent component undergoes evaporation up to this temperature, and the heat-induced intermolecular activity stimulates crystal growth through diffusion and solvent evaporation and, thus, transforms the perovskite yellow phase into a black phase structure by amalgamating the CH_3NH_3I and PbI_2 phases. The TGA curve indicates a weight loss of about 15% between 150 and 250 °C, and the DSC curve indicates the formation of an exothermic peak at 250 °C, which is consistent with the data in Figure 2A and indicates sublimation of the CH_3NH_3I phase and, hence, beginning of the perovskite film degradation after 150 °C. Unlike incomplete decomposition and remaining almost 10% of the mass in Figure 2B, the perovskite precursor DSC−TGA analysis demonstrates complete mass loss for

https://dx.doi.org/10.1021/acsaem.0c01520
ACS Appl. Energy Mater. 2020, 3, 11641−11654

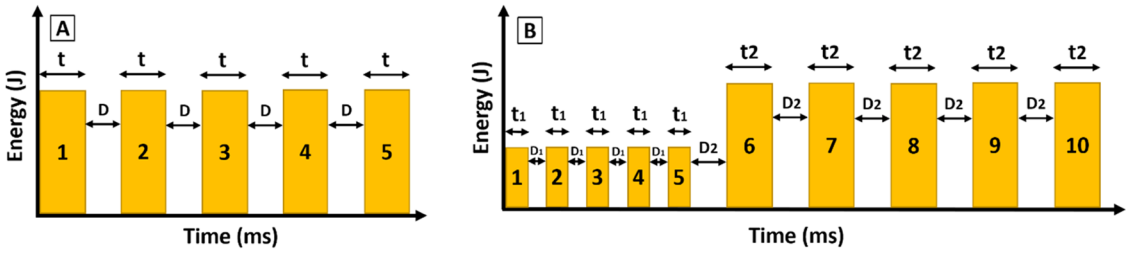

Figure 3. Schematic showing the IPL parameters for (A) UFA and (B) GFA.

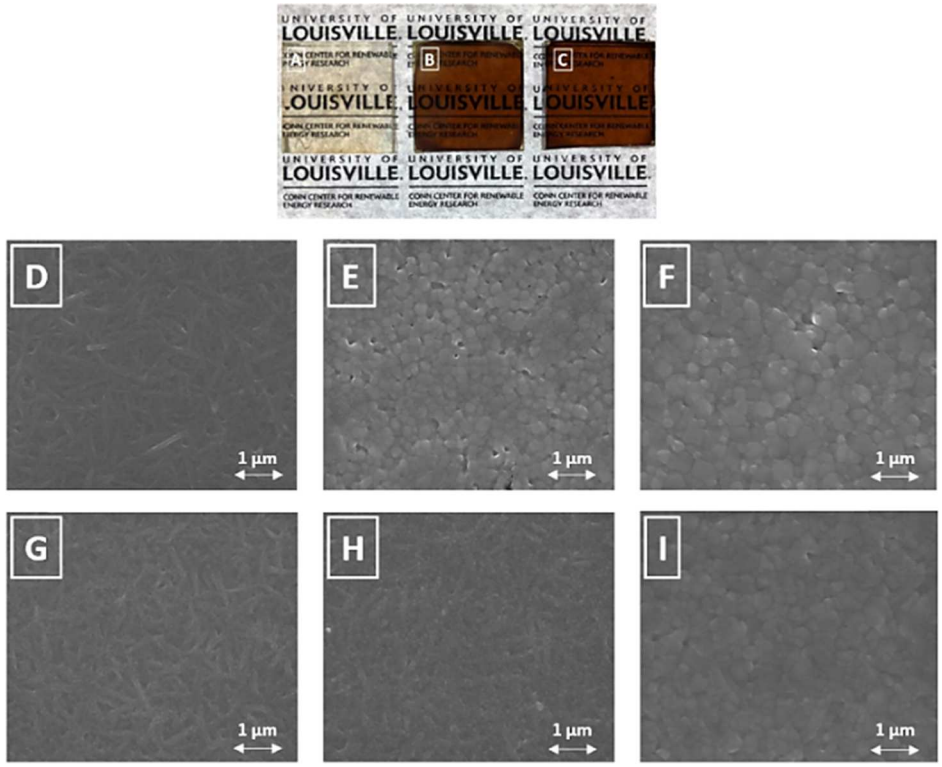

Figure 4. Evolution and top-surface SEM images of the perovskite film (A, D) upon spin-coating and after (B, E) three and (C, F) five flashes through UFA and (G) 10, (H) 20, and (I) 30 s of hotplate annealing.

temperatures higher than 650 °C, which indicates complete elimination of the $CH_3NH_3PbI_3$ perovskite constituents through evaporation. These results indicate that the annealing processes should be carried out in compliance with the perovskite material properties, and the optimal synergy of the applied heat flux and exposure time is pivotal for PSCs maximized stability and efficiency.

To carry out the study, the supersaturated perovskite intermediate was rapidly annealed through uniform and gradient flashing approaches using IPL. The uniform flash annealing (UFA) was carried out by applying five similar flashes, each with the duration and delay time between flashes of t and D, respectively. The gradient flash annealing (GFA) was carried out through two sequential flashing steps consisted of a primary and a secondary annealing step, each consisted of five flashes with a fixed duration of t_1 and t_2 and interval time between flashes of D_1 and D_2, respectively. The flash duration for a constant applied voltage determined the released energy; hence, t_1 was set shorter for the primary annealing to apply lower energy in this step. The schematic indicating the IPL parameters of the two annealing approaches is shown in Figure 3.

The fabrication was initiated by IPL annealing of the SnO_2 ETL similar to our previous work[40] followed by rapid annealing of the perovskite intermediate through IPL. In the first stage, the perovskite films were annealed through UFA by applying only five flashes, each carrying 400 J energy (1.72 J/cm^2) and 1 s delay time between flashes, to anneal the perovskite films in almost 4 s. Figure 4A–C shows the evolution of intermediate phase during IPL annealing. Upon spin-coating, the film was transparent and was associated with the intermediate phase (Figure 4A). Figure 4B shows the quality of perovskite film after applying three flashes, indicating mixed yellow and black phases, and Figure 4C shows the formation of darker films after five flashes. This evolution of the film mimics the transformation results using traditional hotplate annealing techniques.[50] Top-surface SEM images corresponding to the as-deposited, three, and five flashes demonstrate the morphology evolution of the perovskite films annealed through different flash counts (Figure 4D–F). Figure 4D shows the morphology of the intermediate phase formed upon spin-coating. Upon annealing with three flashes, larger crystals with several observable defect states were formed, which indicated that the applied photons were absorbed by the

https://dx.doi.org/10.1021/acsaem.0c01520
ACS Appl. Energy Mater. 2020, 3, 11641–11654

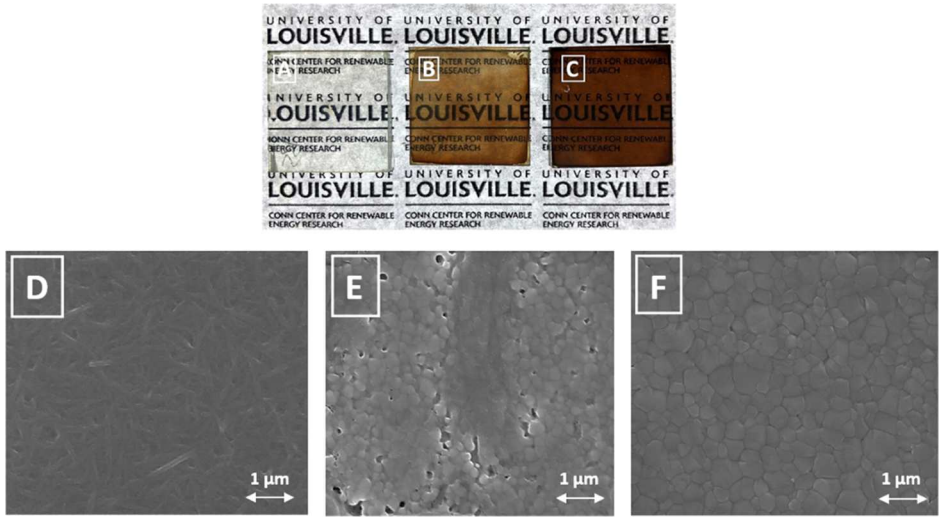

Figure 5. Evolution and top-surface SEM images of the perovskite film (A, D) upon spin-coating and after (B, E) primary and (C, F) secondary annealing steps of GFA.

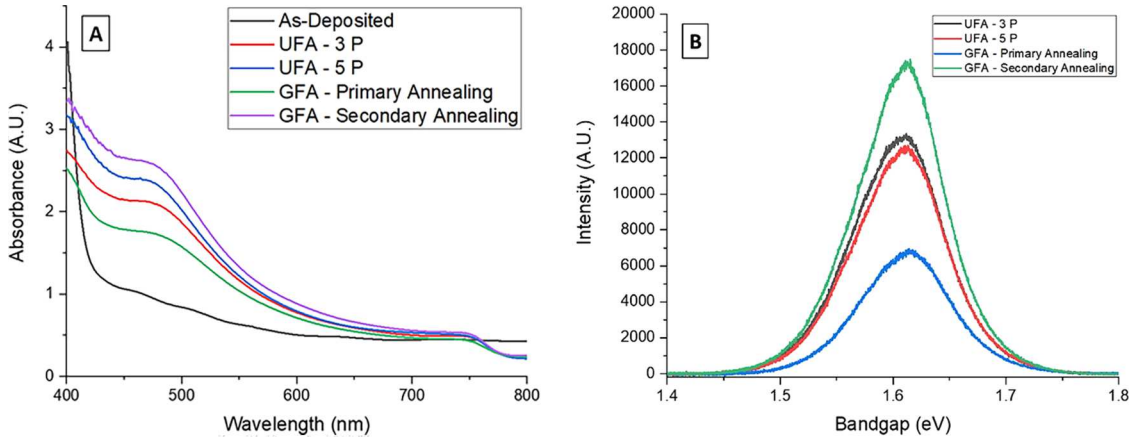

Figure 6. (A) UV−vis spectra and (B) PL peak of the IPL-annealed perovskite films.

intermediate phase, converted to phonons, and aided grain growth through diffusion.[51−55] Further pulse count increase to five resulted in larger grains with very few defects on the surface, and pulse counts more than five damaged the film, which indicates material degradation due to excess annealing. For comparison, Figure 4G−I shows the top-surface SEM images indicating the morphology evolution of perovskite films annealed through 30 s hotplate pre-annealing as was previously introduced to remove the solvents and form the perovskite impure black phase prior to final IPL annealing.[35,40] The images show diminishing dendrites upon further annealing and elimination of the dendrite structures after 30 s. The comparison of short-term hotplate and uniform flash annealed perovskite films delineates similar morphology with a mixture of small and large grains, which indicates that UFA is unable to achieve the desired morphology.

The UFA method was able to anneal the films; however, they were observed to have a more optically matte finish, which would indicate a rougher surface and, hence, unoptimized annealing. To enable controlled annealing, the GFA approach, consisted of consecutive primary and secondary annealing steps, was utilized. In the former step, five flashes each carrying 200 J energy (0.86 J/cm^2) and 250 ms delay time between flashes were applied to the as-deposited perovskite films and five flashes each carrying 400 J energy (1.72 J/cm^2) and 1 s delay time between flashes, similar to UFA, were applied to the films in the latter step to accomplish the perovskite film annealing in about 6 s. Figure 5A−C shows the evolution of perovskite film upon GFA, indicating darker films after each annealing stage. Compared to the indicated morphology in Figure 4B,E, the primary annealing step (Figure 5B) formed a rough pale brown film, which can be attributed to the incomplete formation of the perovskite black phase upon low heat flux exposure in this step. Upon completion of the secondary annealing stage, dark brown films with ultrasmooth quality were obtained, which indicated the formation of the favorable perovskite black phase. To investigate film morphology, top-surface SEM images of the films were obtained and are shown in Figure 5D−F. Similar to the UFA stage, as shown in Figure 5E, the primary annealing stage resulted in small grains with pinholes, indicating incomplete thin film annealing. In addition, the morphology indicated a monolithic ribbon with undetectable grains, which can be attributed to the perovskite intermediate phase. As shown in Figure 5F, upon completion of the secondary annealing step, the entire intermediate phase was eliminated and continuous perovskite morphology with well-developed grains was formed. This indicates gradual consumption of the

https://dx.doi.org/10.1021/acsaem.0c01520
ACS Appl. Energy Mater. 2020, 3, 11641−11654

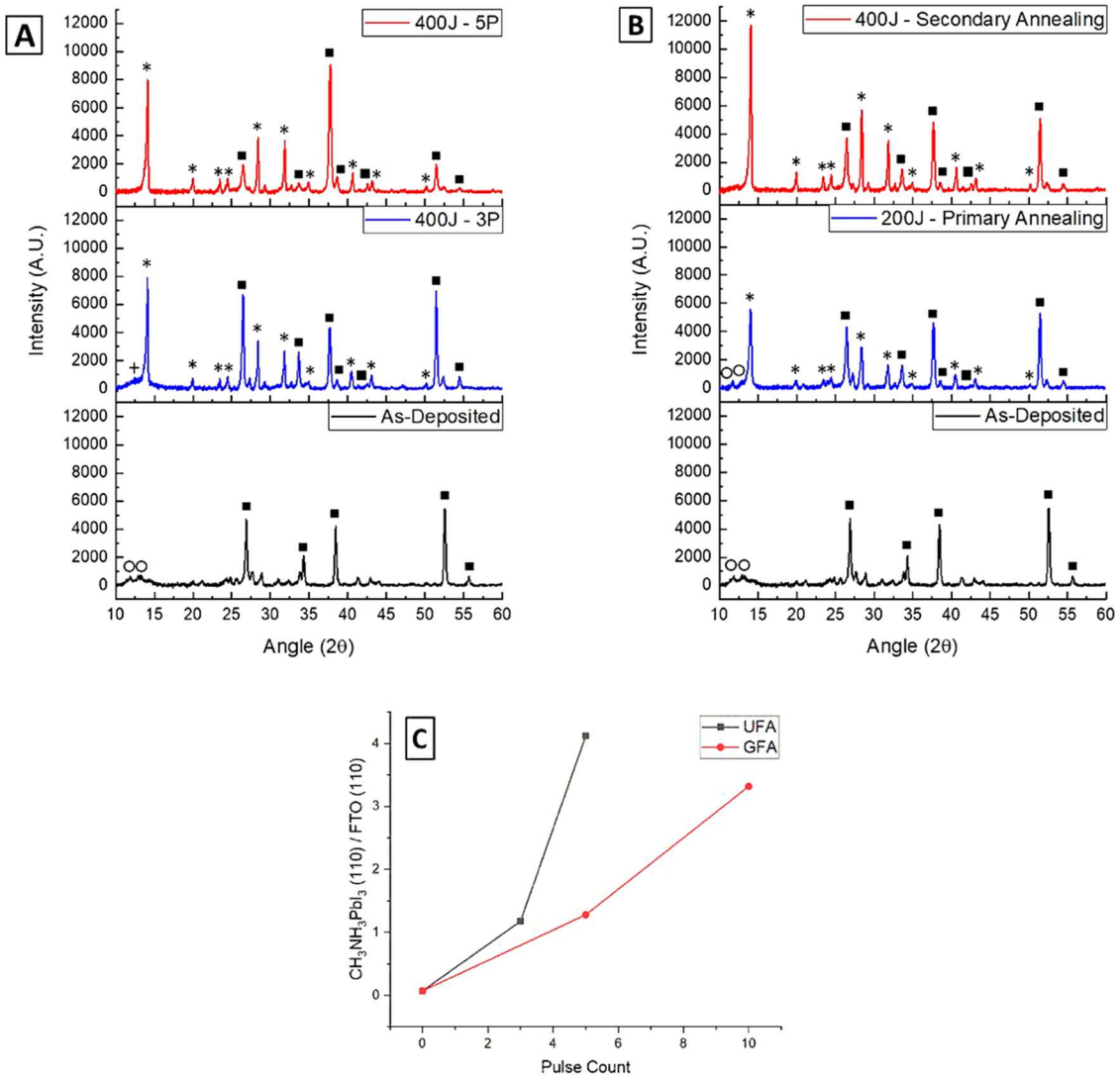

Figure 7. XRD patterns of IPL-annealed perovskite films through (A) UFA and (B) GFA; (C) ratio of perovskite to FTO(110) planes. The peaks marked with ○, ■, +, and * illustrate 2H polytype, FTO/SnO_2, PbI_2, and perovskite black phases, respectively.

intermediate phase to develop grains during the primary and secondary annealing steps, thus transforming the yellow intermediate to the perovskite black phase with superior morphology and conforms with other reports.[51] It can be clearly observed from the top-surface SEM images that the GFA resulted in well-bound grains with more uniformity, which excels the obtained morphology shown in Figure 4F,I with inconsistent grain growth and a mixture of small and large grains.

UV−vis absorption of the perovskite films can provide further information about the morphology and consistency of films over larger areas and the films' ability to absorb the IPL energetic photons. As shown in Figure 6A, the as-deposited film indicated little absorbance within the visible and near-IR range and a high absorption close to the UV spectrum, which can be attributed to the photon absorption by the PbI_2 phase.[56] These films are a challenge to initiate the perovskite film formation as they do not absorb much of the IPL energetic photons. During the IPL process, the films progressively absorbed more of the visible energy, which is consistent with the formation of darker films and elimination of pinholes and defects shown in Figures 4 and 5. However, compared to UFA, the GFA method indicated higher absorption, which indicates the significance of the primary annealing stage contributing to the enhanced phase and morphology of the perovskite film. To better determine the thin film quality, the PL peak of IPL-annealed perovskite films was obtained. As shown in Figure 6B, the perovskite films annealed through GFA depicted the strongest peak, which can be attributed to enhanced charge carrier generation and diminished nonradiative recombination in the annealed film.[57] For all annealing stages, the PL peaks indicated a constant band gap of 1.6 eV, which is consistent with other reports.[57,58] However, the primary annealing stage of GFA demonstrated a slight blue shift with the lowest peak intensity, indicating a higher perovskite band gap due to the least formation of the perovskite black phase at this stage and is consistent with the UV−vis and SEM images shown previously and other reports.[59] These indicate that the primary annealing stage acts as a foundation to initiate solvent evaporation and yields adequate crystal growth throughout the entire annealing process by controlling the diffusion rate and, in turn, the crystallization pace, which is consistent with other reports.[60−62]

Besides morphology, phase evolution is another parameter determining the performance of PSCs. Figure 7A,B shows

https://dx.doi.org/10.1021/acsaem.0c01520
ACS Appl. Energy Mater. 2020, 3, 11641−11654

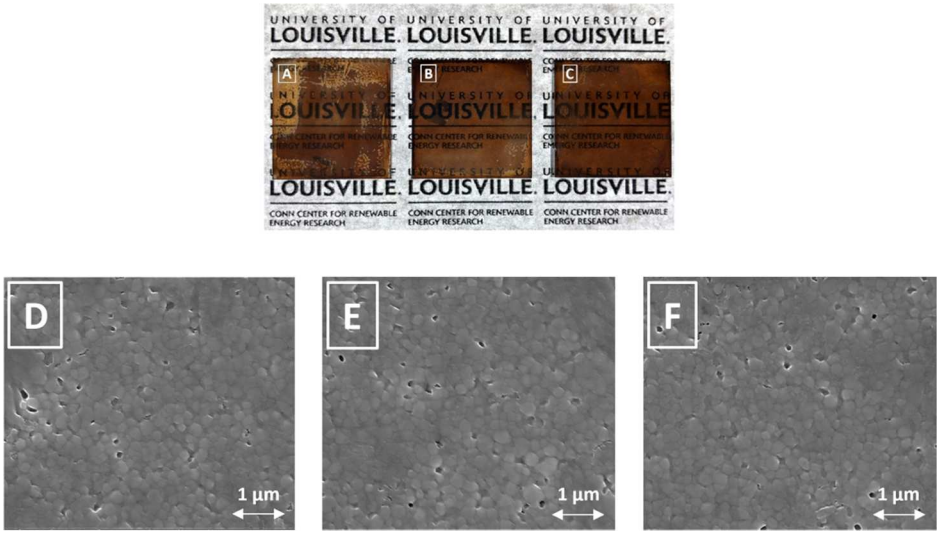

Figure 8. Images indicating the quality of the obtained perovskite black phase for different intervals of (A, D) 100−500 ms; (B, E) 100−1000 ms; and (C, F) 250−500 ms during GFA.

XRD patterns of the FTO/SnO_2/perovskite structure for each annealing stage, where the intense 2θ peaks (marked with •) at around 26.5, 33.7, 37.7, 38.65, 42.5, 51.5, and 54.5° are assigned to the (110), (101), (200), (111), (210), (211), and (220) FTO/SnO_2 tetragonal rutile crystal planes (JCPDS 41-1445) and the peaks (marked with *) at around 14.1, 20, 23.5, 24.45, 28.4, 31.86, 34.94, 40.7, 43.15, and 50.2° are attributed to the (110), (112), (211), (202), (220), (310), (312), (224), (314), and (404) crystal planes, indicating a perovskite tetragonal structure. The distinct low-intensity 2θ peak (marked with ○) for the as-deposited perovskite films at 11.8° is assigned to 2H, and the peaks at 12.95 and 13.25° can be assigned to the 4H Ramsdell notations,[63] indicating a hexagonal crystal system with a $P6_3/mmc$ space group of the perovskite intermediate phase.[64] As shown in Figure 7A, upon annealing through three flashes during UFA, the major perovskite peaks at 14.1 and 28.4° emerged, and the distinctive 2H and 4H polytypes were replaced with a PbI_2 peak (marked with +) at 12.4°, which indicated that the applied heat flux was excessive and, despite transforming the intermediate to the perovskite black phase, resulted in considerable intermediate phase evaporation, particularly the solvents and CH_3NH_3I phase. Further IPL exposure to five flashes increased the intensity of perovskite black peaks and eliminated the intermediate and PbI_2 phases, which indicates fabrication of a 3R(3C) pure black phase polytype. Interestingly, the evolution of perovskite phase during GFA presented a slightly different conversion process. As indicated in Figure 7B, the intermediate phase was remaining after the primary annealing stage and the intensities of the major perovskite black phase peaks were lower compared to those of the three pulse stage during UFA, which is consistent with the evolution of perovskite films shown in Figures 4B and 5B and can be attributed to the lower exposed IPL energy during this stage to retard the evaporation.[51] Upon completion of the GFA process, the developed films revealed 1.45 times enhanced intensity compared to the UFA, which can be attributed to the retarded evaporation and, thus, possible intercalation of the CH_3NH_3I phase to develop the perovskite black phase with better crystallinity. This is consistent with the obtained PL, UV−vis, and SEM images with ununiform grain sizes and defect states for UFA and indicates how the primary annealing step played a significant role in crystallization. Similar to UFA, the resulted films did not reveal any PbI_2 peaks after GFA, which indicates the formation of a pure perovskite black 3R(3C) polytype. Both IPL annealing methods unraveled the 2H → 6H → 3R(3C) conversion sequence and is consistent with other reports.[64] For better clarification, the ratio of the major perovskite (110) plane to the FTO(110) plane is shown in Figure 7C.

To understand how the interval time between flashes influenced the perovskite black phase formation, three different IPL parameters with merely different interval time between flashes were applied. The three conditions had the similar total pulse counts of 10, as well as the 200 J (0.872 J/cm^2) and 400 J (1.74 J/cm^2) energy during GFA, but different interval times of 100−500, 100−1000, and 250−500 ms, in which the first and second values represent the interval times between flashes for the primary and secondary annealing steps, respectively. Figure 8shows the evolution and SEM images of 100−500 ms (A, D) and 100−1000 ms (B, E) interval time conditions for GFA. It can be clearly observed that both interval times were unable to convert the intermediate phase to the perovskite black phase, which, in addition to the results obtained from UFA, indicated that the ultrashort interval time of 100 ms was not providing enough time to evaporate the intermediate liquid phase during annealing. Similarly, as shown in Figure 8C,F, a shorter interval time of 500 ms for the secondary annealing stage revealed a mixture of black and yellow phases with several defect states and undeveloped grains for the 250−500 ms interval time condition, which emphasizes the significance of delay time in solvent evaporation during IPL annealing. Therefore, in addition to heat flux, the rate of solvent evaporation between flashes plays a significant role on tuning the crystallization and formation of a pure perovskite black phase. To further investigate various interval times, XRD patterns delineating the phase purity of the annealed films were obtained, and the results are shown in Figure S1 of the Supporting Information. Similar to the evolution observed in Figure 7, all XRD patterns indicated PbI_2 and 2H intermediate phases upon annealing, indicating inadequate crystallization of the perovskite films when annealed through mentioned intervals. Therefore, we

https://dx.doi.org/10.1021/acsaem.0c01520
ACS Appl. Energy Mater. 2020, 3, 11641−11654

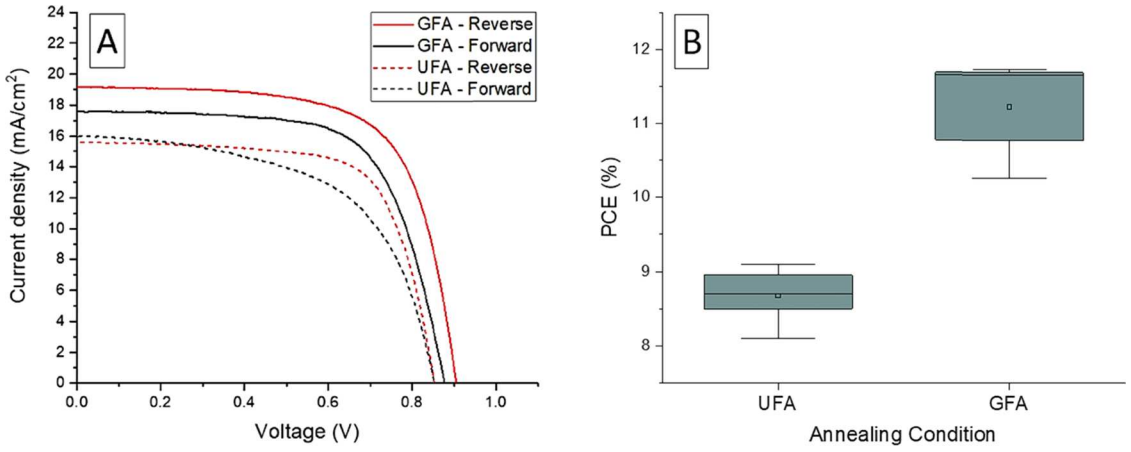

Figure 9. (A) $J-V$ curves of champion cells and (B) box chart exhibiting reverse scan PCE distribution of PSCs annealed through UFA and GFA.

Table 1. Average photovoltaic parameters for five IPL-annealed PSCs through UFA and GFA methods.

annealing method	V_{OC} (V)	J_{SC} (mA/cm^2)	PCE (%)	FF (%)
UFA	0.873 ± 0.016	14.58 ± 0.75	8.67 ± 0.35	68.15 ± 1.72
GFA	0.887 ± 0.017	19.11 ± 0.46	11.23 ± 0.60	66.59 ± 2.16

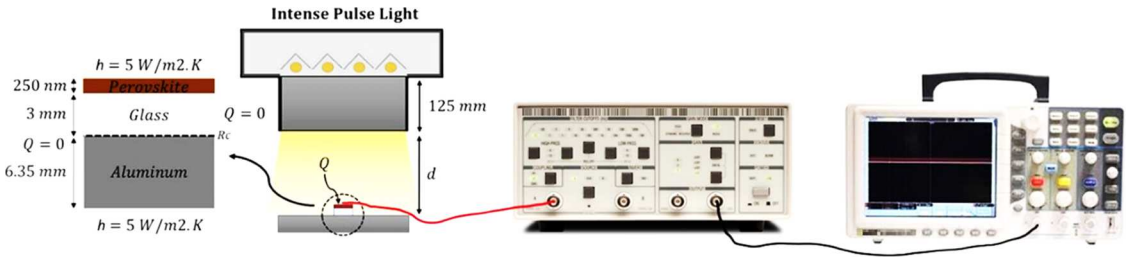

Figure 10. Schematic showing the temperature measurement setup and dimensional illustration of the IPL-annealed PSCs used for transient thermal simulation using ANSYS.

only fabricated the devices and determined the photovoltaic parameters for the UFA and 250−1000 ms interval time condition for the GFA.

The material characterization study indicated successful fabrication of perovskite films for UFA as well as the GFA method with the 250−1000 ms interval time condition. To determine performance, the forward and reverse scan $J-V$ curves indicating the photovoltaic parameters of fabricated PSCs were obtained. As shown in Figure 9, the maximum power conversion efficiency (PCE) of fabricated solar cells was found for the reverse scans exhibiting the open-circuit voltage (V_{OC}), short-circuit current (J_{SC}), power conversion efficiency (PCE), and fill factor (FF) of 0.85 V, 15.59 mA/cm^2, 9.27, and 69.92% for the champion PSC fabricated through UFA and were increased to 0.91 V, 19.17 mA/cm^2, 11.75, and 68% when annealed through GFA, respectively, indicating 26.75% performance improvement for the GFA condition when fabricated in a high-humidity ambient ranging between 60 and 70%. The summary of the photovoltaic parameters for five devices fabricated in each condition is given in Table 1, which indicates average V_{OC}, J_{SC}, PCE, and FF of 0.873 V, 14.58 mA/cm^2, 8.67, and 68.15% for the UFA and 0.8887 V, 19.11 mA/cm^2, 11.23, and 66.59% for the GFA condition, respectively. These are also plotted in Figure 9B, illustrating high reproducibility of the fabricated cells during GFA. Notably, the obtained V_{OC} is lower than the reported values in our previous works, which can be attributed to the Spiro-MeOTAD hole transport material used in this study and conforms with other reports.[65] The statistical results show that the enhanced current density was the most impacting factor on device efficiency, which can be attributed to the enhanced crystallinity and morphology of the perovskite films obtained through the GFA method. The fabricated devices were stable for several weeks when stored in a dark ambient environment. However, a complete device stability study was not undertaken in this work.

2.1. IPL Finite Element Simulation. To better understand the impact of IPL parameters on grain growth and morphology evolution, the flash peak temperature during IPL annealing was measured and compared to a 2D FEA using ANSYS to estimate and validate the peak temperature rise at the perovskite films. The simulation was conducted by modeling flash annealing on perovskite films deposited on glass slides considering a natural convection coefficient of h = 5 W/(m^2·K), Q = 0 W on the sides to carry out one-dimensional heat transfer within the depth direction of the thin film and applying 20% contact resistance, R_c, between glass and aluminum stage which was used to place the slides within d = 75 mm from the lamp during IPL annealing as shown in Figure 10. Further dimensional details are provided in the device fabrication section. IPL annealing of thin films was previously reviewed, and fundamental thermal response equations were discussed.[27] Upon annealing, the IPL is

https://dx.doi.org/10.1021/acsaem.0c01520
ACS Appl. Energy Mater. 2020, 3, 11641−11654

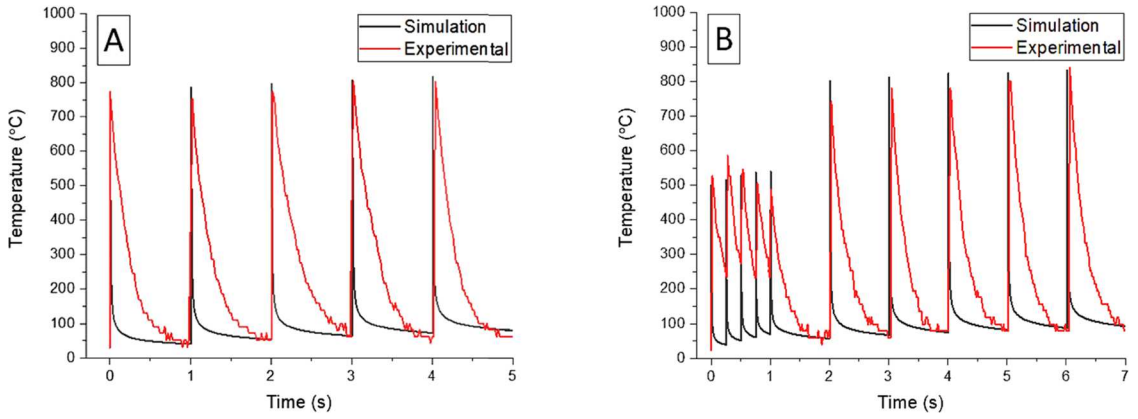

Figure 11. Experimental and numerical results demonstrating the maximum temperature rise occuring at the perovskite film for (A) UFA and (B) GFA.

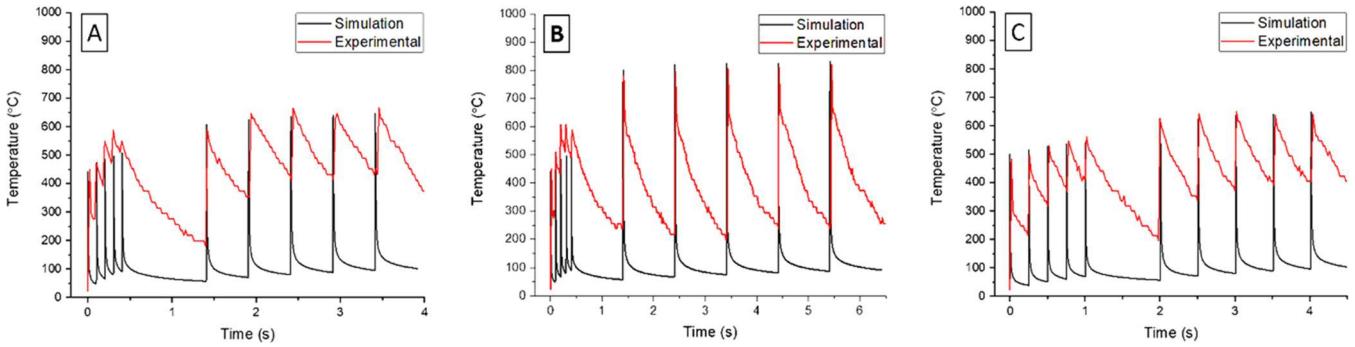

Figure 12. Maximum experimental and numerical temperatures at the surface of the perovskite film when annealed through different delay times between flashes of (A) 100 and 500 ms; (B) 100 and 1000 ms; and (C) 250 and 500 ms for the primary and secondary annealing steps during GFA, respectively.

expected to increase the thin film temperature according to the following one-dimensional transient heat transfer equation

$$\frac{\partial}{\partial z}\left(K\cdot\frac{\partial T}{\partial z}\right) + Q_{abs} = \rho\cdot C_p\cdot\frac{\partial T}{\partial t} \quad (1)$$

where Q_{abs} is the absorbed heat by the perovskite film (W/m^3), K is the thermal conductivity, ρ is the density, and C_p is the specific heat transfer capacity of the perovskite film, which were considered as 1.1 W/(m·K), 4.2864 g/cm^3, and 190 J/(mol·K), respectively.[66−68] Upon flashing, the stored energy in capacitors is discharged to the lamp and the released photons carry energy based on the following equation

$$E_{light} = \left(\frac{V\cdot I}{A}\right)\cdot\eta_{elec} \quad (2)$$

where E_{light} is the photon flux released from the lamp (W/m^2), V is the applied voltage (V), and I is the applied current (Amps) to the Xenon lamp from capacitors. A = 232.26 cm^2 is the illuminating source area, and η_{elec} = 50% is the electrical-to-photon conversion efficiency. The absorbed heat flux by the thin film (Q_{abs}) is the product of the transmitted light energy and distance function (L_d) multiplied by the maximum intersection of the thin film absorbance $A(\lambda)$ and Gaussian fit of the Xenon flash lamp irradiation spectrum $I(\lambda)$ as shown in Figure S2 of the Supporting Information and is defined as

$$Q_{abs} = E_{light}\cdot L_d\cdot(A(\lambda)\cdot I(\lambda))_{max} \quad (3)$$

The above equations indicate that the released energy from capacitors undergoes some loss before being absorbed by the thin film and the temperature rise depends on the photo-absorption capacity of the target thin film.

Figure 11 shows the experimental and simulation results demonstrating the thermal response measured by the thermocouple located on top of the perovskite film during IPL annealing. To obtain thermal response, an oscilloscope was attached to an amplifier, and measurement details pertinent to the setup are provided in the device fabrication section. As shown in Figure 11A, experimental and simulation results for UFA resulted in the peak temperatures between 760 and 820 °C as the flashes progress, and the temperatures measured through the experiment were within less than 5% of the simulation results. The delay time between flashes allowed for the film temperature to recover toward ambient with each subsequent flash increasing this resting temperature about 10−20 °C. The reduction in temperature was primarily a result of the thermal diffusivity ($k/\rho C_p$) and heat capacity (mC_p) of the glass substrate to quickly transfer the heat from the perovskite film. Heat transfer to the surroundings through convection and radiation completed the rapid temperature decline following each flash. The broader temperature signal fall-off for the experimental results is attributed to the high and low pass filtering of the amplifier as well as the mass of thermocouple. Similarly, simulation results indicated peak temperatures between 500 and 540 °C for the primary annealing step and 800 and 830 °C for the secondary annealing step during GFA. In turn, the measured temperatures from the experimental

https://dx.doi.org/10.1021/acsaem.0c01520
ACS Appl. Energy Mater. 2020, 3, 11641−11654

setup indicated the maximum temperatures between 480 and 590 °C for the primary annealing and between 740 and 840 °C for the secondary annealing step, indicating less than 13.6% variation to the simulation results and is consistent with other reports.[69,70] The results indicated that the surface temperature reached to nearly 800 °C, which was over 5 times higher than the 150 °C degradation temperature of the $CH_3NH_3PbI_3$ black phase and even exceeded the 650 °C evaporation temperature of the entire perovskite phases found through TGA/DSC. Therefore, the time-dependent temperature determines the phase and morphology evolution of perovskite films during IPL annealing.

Figure 12 shows the thermal response of the thermocouple placed at the perovskite film surface for the interval times of 100 and 250 ms in the primary annealing step, as well as 500 and 1000 ms in the secondary annealing step. As shown in Figure 12A,C, the ultrashort interval of 100 ms indicated slightly higher temperatures than the 250 ms interval, reaching to almost 600 °C, which indicates the predominating effect of the applied heat flux to natural convection during the delay time on elevating the surface temperature. Surprisingly, the 500 ms interval for the secondary annealing step flashes indicated a lower peak temperature, reaching to about 650 °C at the end of the annealing process and is consistent with the observed poor morphology and incomplete phase transformation in Figure 8. This can be attributed to the hampered solvent evaporation as a result of insufficient delay time between flashes. Notably, the temperature survey of the secondary annealing stage showed in Figure 12B is similar to that in Figure 11B; however, as was previously shown in Figure 8, the 100 ms interval hindered achieving the perovskite pure black phase with superior morphology, which indicates the significance of solvent evaporation and phase transformation between flashes. Despite increasing the surface temperature, ultrashort delay times indicated poor morphology, which is probably due to incomplete diffusion of species at these short time scales. Therefore, a compromise of heat flux and time is necessary to obtain superior morphology and a pure perovskite black phase.

To realize how GFA could enhance the morphology and performance of PSCs, the estimated activation energy for grain boundary mobility was calculated from the following Arrhenius equation[71]

$$M = M_0 \cdot e^{(-E_a/R \cdot T)} \quad (4)$$

where M_0 is the pre-exponential value, E_a is the activation energy for grain boundary mobility (kJ/mol), R = 8.314 J/(mol K) is the gas constant, T is the maximum flash temperature (K), and M is the thermal diffusivity (nm^2/s) determining the grain boundary mobility after flashing and can be described as

$$M = \frac{\varnothing^{1/n} - \varnothing_0^{1/n}}{t} \quad (5)$$

in which, Ø and $Ø_0$ are the average grain diameters after and before IPL annealing, respectively, t is the flash duration, and n = 0.5 is the grain growth exponent found from the logarithmic plot of Ø and t as shown in Figure S3 of the Supporting Information. Upon processing, the ImageJ analysis indicated the average grain sizes of 196 and 251 nm for the perovskite films processed through UFA and the 250−1000 ms condition of GFA, respectively, indicating 28% growth for the latter approach, and the histograms are shown in Figure S4 of the Supporting Information. Similarly, the average grain sizes of perovskite films annealed through three flashes of UFA and the primary step of the GFA were found to be 158 and 150 nm, respectively.

Figure 13 demonstrates the Arrhenius plots for UFA and GFA approaches, in which the slope of graphs is determinative

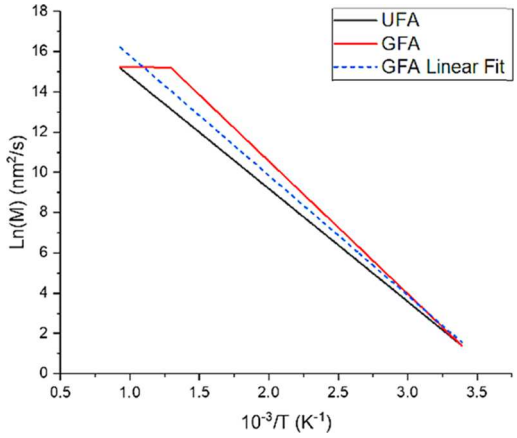

Figure 13. Arrhenius plots for UFA and GFA.

of the grain boundary mobility activation energy. The plots revealed nearby activation energies, indicating one-step increase of 47 kJ/mol during UFA and a two-step increase of 55 kJ/mol followed by a mild slope of 0.5 kJ/mol for the primary and secondary annealing steps during GFA, respectively. These results conform with the illustrated characterization results and can be attributed to the shrinkage of activation energy during GFA, which implemented three significant roles to enhance the PSC performance. First, the lower applied temperature during the primary annealing step of GFA mitigated the diffusion rate according to Fick's law of diffusion[51] and, in turn, enabled controlled grain growth. Second, in addition to the diminished diffusion rate, the primary step during GFA retarded the crystallization pace as a result of providing longer overall annealing time of about 6 s during the GFA approach compared to 4 s during UFA. Third, unlike UFA that rapidly induced high temperatures in a shorter time, the Arrhenius plot shrinkage during GFA regulated solvent evaporation and, thus, enabled adequate solvent evaporation with respect to phase transformation during annealing, which is consistent with the delineated phase transformation through XRD. The synergy of all of these parameters indicates how the exerted photon flux and time through GFA could improve the perovskite morphology and impact PSC performance.

3. CONCLUSIONS

The rapid fabrication of PSCs entirely through IPL annealing was introduced by comparing the UFA with the phased GFA approach consisted of primary and secondary annealing steps. The maximum device efficiency enhanced from 9.27 to 11.75% when a primary annealing step with energy flux as low as 200 J/pulse (0.89 J/cm²) was applied before the secondary annealing step with 400 J/pulse (1.78 J/cm²). The simulation and experimental results indicated identical maximum temperature rise during each flashing, surpassing 800 °C, which conformed with characterization results and PSC performance.

https://dx.doi.org/10.1021/acsaem.0c01520
ACS Appl. Energy Mater. 2020, 3, 11641−11654

The lower performance of PSCs processed through UFA was attributed to the obtained low-quality perovskite morphology as a result of one-step IPL application, exerting intense activation energy on the as-deposited perovskite films, to rapidly evaporate the intermediate phases before being consumed for perovskite black formation. In contrast, the higher performance of PSCs annealed through GFA was attributed to the regulated atomic diffusion rate to retard the crystallization pace as a result of activation energy shrinkage, exerting 55 and 0.5 kJ/mol for the primary and secondary annealing steps during GFA, respectively. In addition to the photothermal effect, the interval time between flashes determined the phase transformation and morphology evolution during IPL annealing. Ultrashort interval of 100 ms increased the surface temperature but was unable to provide superior perovskite black phase upon annealing, which signified the importance of solvent evaporation between flashes. Similarly, despite exceeding 650 °C, the shorter interval time of 500 ms for the secondary annealing stage impeded the formation of the pure perovskite black phase with ultrasmooth morphology as a result of insufficient solvent evaporation during IPL annealing. The GFA approach led to better performance as a result of obtaining better perovskite morphologies through retarded crystallization, regulated atomic diffusion rate, and sufficient evaporation between each flashing. The utilization of GFA technique reduced the entire PSC annealing time to about 10 s after deposition. Future studies should consider the impact of IPL processing parameters on the durability of PSCs. This study establishes a promising pathway for researchers and industries to take the advantage of IPL to achieve low-cost, large-scale, and high-speed fabrication of semiconductors and photovoltaics.

4. EXPERIMENTAL SECTION

4.1. Materials. Lead(II) iodide (99.99%, trace metals basis) was purchased from TCI, di-iodomethane (99%) and SnO_2 solution (15% in H_2O colloidal dispersion) were purchased from Alfa Aesar. Methylammonium iodide (MAI) and cobalt dopant FK209 were purchased from Greatcell Solar. The 2,2′,7,7′-tetrakis[*N*,*N*-di(4-methoxyphenyl)amino]-9,9′-spirobifluorene (99%, Spiro-MeOTAD) was acquired from Lumtec. FTO glass slides (<20 Ω/sq, 2 cm × 2 cm × 3 mm) and gold pellets (99.999%) were purchased from Hartford Glass and Kurt J. Lesker Co., respectively. All other materials were purchased from Sigma Aldrich and used without further purification.

4.2. Device Fabrication. FTO glass slides were etched using zinc powder and 2M HCl and were later cleaned through 10 min individual sonication in a 1:10 V/V diluted solution of Hellmanex detergent in deionized (DI) water, DI water, ethanol, and DI water, respectively. After blowing with nitrogen to remove the remainder water, plasma treatment was conducted to enhance the hydrophilicity of the FTO glass slides. The SnO_2 ETL was then spin-coated from a 1:4 V/V diluted solution of the SnO_2 colloidal dispersion in fresh DI water using a spinning rate of 2000 rpm for 30 s. Before annealing, the electrode locations covered with SnO_2 were wiped using cotton swabs dipped in DI water and were immediately transferred to the IPL machine (Sinteron S-2210, Xenon Corp.) equipped with 4 linear lamps for rapid annealing through 5 flashes, each carrying 2.1 kJ energy and 1 s delay time between flashes similar to our previous work.[40] The reflected energy was adjusted by applying 2121 V to the lamp and adjusting the flash duration to 2 ms. After annealing, the slides were treated through UV to provide surface treatment and remove the organic contaminants for 5 min. The perovskite ink was then passed through a 0.45 μm PTFE syringe filter and coated on the SnO_2-coated slides using a spin coater supplied with dry air to keep the relative humidity less than 10% through two consecutive spinning steps of 1000 rpm for 3 s and 4000 rpm for 25 s to provide a 250 nm thick perovskite film after annealing. During the last 10 s of the spinning process, 100 μL of chlorobenzene was pipetted on the rotating substrate to form the perovskite intermediate phase. The $CH_3NH_3PbI_3$ perovskite precursor was made in a nitrogen-filled glovebox according to our previously reported recipe.[35] In brief, 0.6454 g of PbI_2 and 0.2226 g of CH_3NH_3I were initially dissolved in 1 mL of DMF and 0.125 mL of DMSO. Upon complete dissolution and formation of the transparent yellow precursor, 0.25 mL of di-iodomethane was added to the solution and stirred for 2 h. Right after spin-coating, the electrode locations were wiped using cotton swaps dipped in DMF and were immediately annealed through IPL in the ambient environment with relative humidity ranging between 60 and 70%. The IPL annealing was conducted after putting the slides on a linear stage equipped with a 6.35 mm thickness aluminum platform and was lifted to maintain a distance of d = 75 mm from the 125 mm extruded section attached to the lamp chamber to avoid light scattering to the ambient. Both platform and extruded part had a square cross section with 150 mm side length. The UFA was conducted through 3 and 5 flashes, each carrying 400 J energy. The GFA was conducted through consecutive primary and secondary annealing steps. The primary annealing was conducted through 5 flashes, each carrying 200 J energy and 250 ms delay time between flashes, and the secondary annealing was carried out similar to UFA. For both annealing methods, the applied voltage to the lamp was set to 1737 V and the flashing duration was set to 1125 and 1982 μs to reflect the desired energies of 200 and 400 J per flash, respectively. Right after perovskite annealing, the substrates were transferred to a nitrogen-filled glovebox for Spiro-MeOTAD hole transport layer coating. The Spiro-MeOTAD solution was made by mixing 72.3 mg of Spiro-MeOTAD, 28.8 μL of 4-*tert*-butyl-pyridine, 17.5 μL of a stock solution of 520 mg/mL lithium bis (trifluoromethylsulfonyl) imide in anhydrous acetonitrile, and 29 μL of the cobalt dopant FK209 TFSI salt (300 mg/mL in anhydrous acetonitrile) in 1 mL of anhydrous chlorobenzene. The Spiro-MeOTAD film was made by spin-coating 70 μL of the prepared solution at 1700 rpm for 30 s to obtain 200 nm thickness. Finally, a 70 nm gold electrode was deposited through a thermal evaporator.

4.3.. Temperature Measurement. The estimated maximum temperature at the perovskite film surface during IPL annealing was measured using a K-type thermocouple consisted of a Chromel and an Alumel wire (0.08 mm, Omega engineering) joint together through a hot junction and was kept tangent to the thin film surface to measure the photon temperature occurring at the film. The thermocouple was connected to a 300 MHz, 2.5 GSa/s high-speed oscilloscope (DS 8302, Owon smart) via a low noise amplifier (SR560, Stanford Research Systems) with a gain of 100× to measure the generated voltage during flashing. The obtained voltage was then converted to reflect the temperature rise during flash annealing.

4.4. Characterization. XRD measurements were obtained at the 2θ range between 10 and 60° using a Bruker AXS D8 X-ray diffractometer equipped with a position sensitive detector (PCD) and an X-ray source of Cu Kα (λ = 0.1548 nm) with a scanning speed of 1 s/step and a step size of 0.02°. Surface morphology inspections were done through a FEI Nova NanoSEM 600 machine with an accelerating voltage of 10 kV and a working distance of 5 mm. The current−voltage curves were obtained using an Autolab PGSTAT128-N potentiostat with a scanning rate of 0.1 V/sec. Each cell was illuminated from the back side with an active area of 0.12 cm^2 using an AM 1.5 simulated light from a Newport LCS-100 solar simulator. The transmission and absorption spectra were obtained using a PerkinElmer Lambda 950 UV−vis spectrometer between 250 and 800 nm wavelengths. PL analysis was carried out using a Renishaw inVia Raman microscope with a CCD detector and a 632 nm He−Ne laser source.

■ ASSOCIATED CONTENT

Supporting Information

The Supporting Information is available free of charge at https://pubs.acs.org/doi/10.1021/acsaem.0c01520.

https://dx.doi.org/10.1021/acsaem.0c01520
ACS Appl. Energy Mater. 2020, 3, 11641−11654

XRD patterns of perovskite films annealed through different delay times during GFA, xenon flash lamp irradiation spectrum and intersection of its Gaussian fit with UV−vis spectra of perovskite films, logarithmic plot of grain size versus IPL duration for UFA and GFA, and histograms of perovskite grain sizes (PDF)

AUTHOR INFORMATION

Corresponding Author

Thad Druffel − *Conn Center for Renewable Energy Research, University of Louisville, Louisville, Kentucky 40292, United States;* orcid.org/0000-0002-1412-3023; Email: thad.druffel@louisville.edu

Authors

Amir H. Ghahremani − *Conn Center for Renewable Energy Research and Department of Mechanical Engineering, University of Louisville, Louisville, Kentucky 40292, United States*

Sahar Pishgar − *Conn Center for Renewable Energy Research, University of Louisville, Louisville, Kentucky 40292, United States*

Jitendra Bahadur − *Madanapalle Institute of Technology and Science, Madanapalle, Andhra Pradesh 517325, India*

Complete contact information is available at: https://pubs.acs.org/10.1021/acsaem.0c01520

Funding

This work is funded in part or whole by the U.S. National Science Foundation (NSF) award #1828355 and U.S. Department of Energy (DoE) Solar Energy Technologies Office Award #DE-EE0008752.

Notes

The authors declare no competing financial interest.

ACKNOWLEDGMENTS

The authors acknowledge the Conn Center for Renewable Energy Research at the University of Louisville, KY, U.S.A., for providing research facilities.

REFERENCES

(1) Ma, C.; Clark, S.; Liu, Z.; Liang, L.; Firdaus, Y.; Tao, R.; Han, A.; Liu, X.; Li, L. J.; Anthopoulos, T. D.; Hersam, M. C.; Wu, T. Solution-Processed Mixed-Dimensional Hybrid Perovskite/Carbon Nanotube Electronics. *ACS Nano* **2020**, *14*, 3969−3979.

(2) Sichert, J. A.; Hemmerling, A.; Cardenas-Daw, C.; Urban, A. S.; Feldmann, J. Tuning the Optical Bandgap in Layered Hybrid Perovskites through Variation of Alkyl Chain Length. *APL Mater.* **2019**, *7*, No. 041116.

(3) Han, T. H.; Tan, S.; Xue, J.; Meng, L.; Lee, J. W.; Yang, Y. Interface and Defect Engineering for Metal Halide Perovskite Optoelectronic Devices. *Adv. Mater.* **2019**, *31*, No. 1803515.

(4) Chu, W.; Zheng, Q.; Prezhdo, O. V.; Zhao, J.; Saidi, W. A. Low-Frequency Lattice Phonons in Halide Perovskites Explain High Defect Tolerance toward Electron-Hole Recombination. *Sci. Adv.* **2020**, *6*, No. eaaw7453.

(5) Liu, Y.; Wang, J.; Zhu, N.; Liu, W.; Wu, C.; Liu, C.; Xiao, L.; Chen, Z.; Wang, S. Investigation on Binding Energy and Reduced Effective Mass of Exciton in Organic−Inorganic Hybrid Lead Perovskite Films by a Pure Optical Method. *Opt. Lett.* **2019**, *44*, 3474−3477.

(6) Chen, B.; Baek, S.-W.; Hou, Y.; Aydin, E.; De Bastiani, M.; Scheffel, B.; Proppe, A.; Huang, Z.; Wei, M.; Wang, Y.-K. Enhanced Optical Path and Electron Diffusion Length Enable High-Efficiency Perovskite Tandems. *Nat. Commun.* **2020**, *11*, No. 1257.

(7) Green, M. A.; Dunlop, E. D.; Hohl-Ebinger, J.; Yoshita, M.; Kopidakis, N.; Hao, X. Solar Cell Efficiency Tables (Version 56). *Prog. Photovoltaics* **2020**, *28*, 629−638.

(8) Shockley, W.; Queisser, H. J. Detailed Balance Limit of Efficiency of P-N Junction Solar Cells. *J. Appl. Phys.* **1961**, *32*, 510−519.

(9) Druffel, T.; Lavery, B.; Ankireddy, K.; Ghahremani, A. H.; Martin, B.; Gupta, G. Methods for Forming a Perovskite Solar Cell. U.S. Patent US20200127205A12020.

(10) Remeika, M.; Raga, S. R.; Zhang, S.; Qi, Y. Transferrable Optimization of Spray-Coated PbI2 Films for Perovskite Solar Cell Fabrication. *J. Mater. Chem. A* **2017**, *5*, 5709−5718.

(11) Liu, D.; Wu, L.; Li, C.; Ren, S.; Zhang, J.; Li, W.; Feng, L. Controlling CH3NH3PbI3−XClX Film Morphology with Two-Step Annealing Method for Efficient Hybrid Perovskite Solar Cells. *ACS Appl. Mater. Interfaces* **2015**, *7*, 16330−16337.

(12) Guo, F.; He, W.; Qiu, S.; Wang, C.; Liu, X.; Forberich, K.; Brabec, C. J.; Mai, Y. Sequential Deposition of High-Quality Photovoltaic Perovskite Layers via Scalable Printing Methods. *Adv. Funct. Mater.* **2019**, *29*, No. 1900964.

(13) Xiao, M.; Zhao, L.; Geng, M.; Li, Y.; Dong, B.; Xu, Z.; Wan, L.; Li, W.; Wang, S. Selection of an Anti-Solvent for Efficient and Stable Cesium-Containing Triple Cation Planar Perovskite Solar Cells. *Nanoscale* **2018**, *10*, 12141−12148.

(14) Chueh, C.-C.; Liao, C.-Y.; Zuo, F.; Williams, S. T.; Liang, P.-W.; Jen, A. K.-Y. The Roles of Alkyl Halide Additives in Enhancing Perovskite Solar Cell Performance. *J. Mater. Chem. A* **2015**, *3*, 9058−9062.

(15) Wu, H.; Zhang, C.; Ding, K.; Wang, L.; Gao, Y.; Yang, J. Efficient Planar Heterojunction Perovskite Solar Cells Fabricated by in-Situ Thermal-Annealing Doctor Blading in Ambient Condition. *Org. Electron.* **2017**, *45*, 302−307.

(16) You, J.; Yang, Y.; Hong, Z.; Song, T.-B.; Meng, L.; Liu, Y.; Jiang, C.; Zhou, H.; Chang, W.-H.; Li, G. Moisture Assisted Perovskite Film Growth for High Performance Solar Cells. *Appl. Phys. Lett.* **2014**, *105*, No. 183902.

(17) Mehdi, H.; Mhamdi, A.; Bouazizi, A. Effect of Annealing Treatment on the Properties of Inverted Solar Cells Based on Mixed Halide Perovskite. *Phys. E* **2020**, *119*, No. 114000.

(18) Li, Z.; Zhao, Y.; Wang, X.; Sun, Y.; Zhao, Z.; Li, Y.; Zhou, H.; Chen, Q. Cost Analysis of Perovskite Tandem Photovoltaics. *Joule* **2018**, *2*, 1559−1572.

(19) Bruening, K.; Dou, B.; Simonaitis, J.; Lin, Y.-Y.; van Hest, M. F.; Tassone, C. J. Scalable Fabrication of Perovskite Solar Cells to Meet Climate Targets. *Joule* **2018**, *2*, 2464−2476.

(20) Sánchez, S.; Jerónimo-Rendon, J.; Saliba, M.; Hagfeldt, A. Highly Efficient and Rapid Manufactured Perovskite Solar Cells via Flash Infrared Annealing. *Mater. Today* **2020**, *35*, 9−15.

(21) Sanchez, S.; Hua, X.; Phung, N.; Steiner, U.; Abate, A. Flash Infrared Annealing for Antisolvent-Free Highly Efficient Perovskite Solar Cells. *Adv. Energy Mater.* **2018**, *8*, No. 1702915.

(22) Ouyang, Z.; Yang, M.; Whitaker, J. B.; Li, D.; van Hest, M. F. Toward Scalable Perovskite Solar Modules Using Blade Coating and Rapid Thermal Processing. *ACS Appl. Energy Mater.* **2020**, *3*, 3714−3720.

(23) Martin, B.; Yang, M.; Bramante, R. C.; Amerling, E.; Gupta, G.; van Hest, M. F.; Druffel, T. Fabrication of Flexible Perovskite Solar Cells via Rapid Thermal Annealing. *Mater. Lett.* **2020**, *276*, No. 128215.

(24) You, P.; Li, G.; Tang, G.; Cao, J.; Yan, F. Ultrafast Laser-Annealing of Perovskite Films for Efficient Perovskite Solar Cells. *Energy Environ. Sci.* **2020**, *13*, 1187−1196.

(25) Singh, M.; Rana, S.; Agarwal, S. Light Induced Morphological Reforms in Thin Film of Advanced Nano-Materials for Energy Generation: A Review. *Opt. Laser Technol.* **2020**, *129*, No. 106284.

(26) Ghahremani, A. H.; Martin, B.; Ankireddy, K.; Druffel, T. Rapid Processing of Perovskite Solar Cells through Pulsed Photonic Annealing: A Review. *J. Coat. Technol. Res.* **2019**, *16*, 1637−1642.
(27) Druffel, T.; Dharmadasa, R.; Lavery, B. W.; Ankireddy, K. Intense Pulsed Light Processing for Photovoltaic Manufacturing. *Sol. Energy Mater. Sol. Cells* **2018**, *174*, 359−369.
(28) Nam, H. J.; Kang, S. Y.; Park, J. Y.; Choa, S.-H. Intense Pulse Light Sintering of an Ag Microparticle-Based, Highly Stretchable, and Conductive Electrode. *Microelectron. Eng.* **2019**, *215*, No. 111012.
(29) Bahadur, J.; Ghahremani, A. H.; Martin, B.; Druffel, T.; Sunkara, M. K.; Pal, K. Solution Processed Mo Doped SnO2 as an Effective ETL in the Fabrication of Low Temperature Planer Perovskite Solar Cell under Ambient Conditions. *Org. Electron.* **2019**, *67*, 159−167.
(30) Kim, K.-S.; Son, E.-W.; Youn, J. W.; Kim, D. U. Intense Pulsed Light Sintering of Vanadium Dioxide Nanoparticle Films and Their Optical Properties for Thermochromic Smart Window. *Mater. Des.* **2019**, *176*, No. 107838.
(31) Dharmadasa, R.; Lavery, B.; Dharmadasa, I.; Druffel, T. Intense Pulsed Light Treatment of Cadmium Telluride Nanoparticle-Based Thin Films. *ACS Appl. Mater. Interfaces* **2014**, *6*, 5034−5040.
(32) Zhu, M.; Liu, W.; Ke, W.; Clark, S.; Secor, E. B.; Song, T.-B.; Kanatzidis, M. G.; Li, X.; Hersam, M. C. Millisecond-Pulsed Photonically-Annealed Tin Oxide Electron Transport Layers for Efficient Perovskite Solar Cells. *J. Mater. Chem. A* **2017**, *5*, 24110−24115.
(33) Dharmadasa, R.; Jha, M.; Amos, D. A.; Druffel, T. Room Temperature Synthesis of a Copper Ink for the Intense Pulsed Light Sintering of Conductive Copper Films. *ACS Appl. Mater. Interfaces* **2013**, *5*, 13227−13234.
(34) Lavery, B. W.; Kumari, S.; Konermann, H.; Draper, G. L.; Spurgeon, J.; Druffel, T. Intense Pulsed Light Sintering of CH3NH3PbI3 Solar Cells. *ACS Appl. Mater. Interfaces* **2016**, *8*, 8419−8426.
(35) Ankireddy, K.; Ghahremani, A. H.; Martin, B.; Gupta, G.; Druffel, T. Rapid Thermal Annealing of CH3NH3PbI3 Perovskite Thin Films by Intense Pulsed Light with Aid of Diiodomethane Additive. *J. Mater. Chem. A* **2018**, *6*, 9378−9383.
(36) Troughton, J.; Carnie, M. J.; Davies, M. L.; Charbonneau, Cc.; Jewell, E. H.; Worsley, D. A.; Watson, T. M. Photonic Flash-Annealing of Lead Halide Perovskite Solar Cells in 1 ms. *J. Mater. Chem. A* **2016**, *4*, 3471−3476.
(37) Polino, G.; Shanmugam, S.; Bex, G. J.; Abbel, R.; Brunetti, F.; Di Carlo, A.; Andriessen, R.; Galagan, Y. Photonic Flash Sintering of Ink-Jet-Printed Back Electrodes for Organic Photovoltaic Applications. *ACS Appl. Mater. Interfaces* **2016**, *8*, 2325−2335.
(38) Galagan, Y.; Coenen, E. W.; Abbel, R.; van Lammeren, T. J.; Sabik, S.; Barink, M.; Meinders, E. R.; Andriessen, R.; Blom, P. W. Photonic Sintering of Inkjet Printed Current Collecting Grids for Organic Solar Cell Applications. *Org. Electron.* **2013**, *14*, 38−46.
(39) Das, S.; Yang, B.; Gu, G.; Joshi, P. C.; Ivanov, I. N.; Rouleau, C. M.; Aytug, T.; Geohegan, D. B.; Xiao, K. High-Performance Flexible Perovskite Solar Cells by Using a Combination of Ultrasonic Spray-Coating and Low Thermal Budget Photonic Curing. *ACS Photonics* **2015**, *2*, 680−686.
(40) Ghahremani, A. H.; Martin, B.; Gupta, A.; Bahadur, J.; Ankireddy, K.; Druffel, T. Rapid Fabrication of Perovskite Solar Cells through Intense Pulse Light Annealing of SnO2 and Triple Cation Perovskite Thin Films. *Mater. Des.* **2020**, *185*, No. 108237.
(41) Lee, J. W.; Lee, D. K.; Jeong, D. N.; Park, N. G. Control of Crystal Growth toward Scalable Fabrication of Perovskite Solar Cells. *Adv. Funct. Mater.* **2019**, *29*, No. 1807047.
(42) Hu, H.; Ren, Z.; Fong, P. W.; Qin, M.; Liu, D.; Lei, D.; Lu, X.; Li, G. Room-Temperature Meniscus Coating of> 20% Perovskite Solar Cells: A Film Formation Mechanism Investigation. *Adv. Funct. Mater.* **2019**, *29*, No. 1900092.
(43) Ahn, N.; Son, D.-Y.; Jang, I.-H.; Kang, S. M.; Choi, M.; Park, N.-G. Highly Reproducible Perovskite Solar Cells with Average Efficiency of 18.3% and Best Efficiency of 19.7% Fabricated via Lewis Base Adduct of Lead (II) Iodide. *J. Am. Chem. Soc.* **2015**, *137*, 8696−8699.
(44) Yousuf, M.; Frawley, P. J. Secondary Nucleation from Nuclei Breeding and Its Quantitative Link with Fluid Shear Stress in Mixing: A Potential Approach for Precise Scale-up in Industrial Crystallization. *Org. Process Res. Dev.* **2019**, *23*, 926−934.
(45) Dualeh, A.; Gao, P.; Seok, S. I.; Nazeeruddin, M. K.; Grätzel, M. Thermal Behavior of Methylammonium Lead-Trihalide Perovskite Photovoltaic Light Harvesters. *Chem. Mater.* **2014**, *26*, 6160−6164.
(46) Kim, J.; Lee, S.-H.; Lee, J. H.; Hong, K.-H. The Role of Intrinsic Defects in Methylammonium Lead Iodide Perovskite. *J. Phys. Chem. Lett.* **2014**, *5*, 1312−1317.
(47) Lee, Y. H.; Luo, J.; Humphry-Baker, R.; Gao, P.; Grätzel, M.; Nazeeruddin, M. K. Unraveling the Reasons for Efficiency Loss in Perovskite Solar Cells. *Adv. Funct. Mater.* **2015**, *25*, 3925−3933.
(48) Liu, Y.; Yang, Z.; Cui, D.; Ren, X.; Sun, J.; Liu, X.; Zhang, J.; Wei, Q.; Fan, H.; Yu, F. Two-Inch-Sized Perovskite CH3NH3PbX3 (X= Cl, Br, I) Crystals: Growth and Characterization. *Adv. Mater.* **2015**, *27*, 5176−5183.
(49) Zhang, W.; Saliba, M.; Moore, D. T.; Pathak, S. K.; Hörantner, M. T.; Stergiopoulos, T.; Stranks, S. D.; Eperon, G. E.; Alexander-Webber, J. A.; Abate, A. Ultrasmooth Organic−Inorganic Perovskite Thin-Film Formation and Crystallization for Efficient Planar Heterojunction Solar Cells. *Nat. Commun.* **2015**, *6*, No. 6142.
(50) Wang, Y. C.; Chang, J.; Zhu, L.; Li, X.; Song, C.; Fang, J. Electron-Transport-Layer-Assisted Crystallization of Perovskite Films for High-Efficiency Planar Heterojunction Solar Cells. *Adv. Funct. Mater.* **2018**, *28*, No. 1706317.
(51) Cao, X.; Zhi, L.; Li, Y.; Fang, F.; Cui, X.; Ci, L.; Ding, K.; Wei, J. Fabrication of Perovskite Films with Large Columnar Grains via Solvent-Mediated Ostwald Ripening for Efficient Inverted Perovskite Solar Cells. *ACS Appl. Energy Mater.* **2018**, *1*, 868−875.
(52) Pham, N. D.; Tiong, V. T.; Yao, D.; Martens, W.; Guerrero, A.; Bisquert, J.; Wang, H. Guanidinium Thiocyanate Selective Ostwald Ripening Induced Large Grain for High Performance Perovskite Solar Cells. *Nano Energy* **2017**, *41*, 476−487.
(53) Yang, M.; Zhang, T.; Schulz, P.; Li, Z.; Li, G.; Kim, D. H.; Guo, N.; Berry, J. J.; Zhu, K.; Zhao, Y. Facile Fabrication of Large-Grain $CH_3NH_3PbI_{3-X}Br_X$ Films for High-Efficiency Solar Cells via CH3NH3Br-Selective Ostwald Ripening. *Nat. Commun.* **2016**, *7*, No. 12305.
(54) Yang, Y.; Wu, J.; Wang, X.; Guo, Q.; Liu, X.; Sun, W.; Wei, Y.; Huang, Y.; Lan, Z.; Huang, M. Suppressing Vacancy Defects and Grain Boundaries via Ostwald Ripening for High-Performance and Stable Perovskite Solar Cells. *Adv. Mater.* **2019**, No. 1904347.
(55) Li, S.; Hu, L.; Zhang, C.; Wu, Y.; Liu, Y.; Sun, Q.; Cui, Y.; Hao, Y.; Wu, Y. In-Situ Growth of 2D/3D Mixture Perovskite Interface Layer by Seed-Mediated and Solvent-Assisted Ostwald Ripening for Stable and Efficient Photovoltaics. *J. Mater. Chem. C* **2020**, *8*, 2425−2435.
(56) Eze, V. O.; Lei, B.; Mori, T. Air-Assisted Flow and Two-Step Spin-Coating for Highly Efficient CH3NH3PbI3 Perovskite Solar Cells. *Jpn. J. Appl. Phys.* **2016**, *55*, No. 02BF08.
(57) Wang, J.; Zhang, J.; Zhou, Y.; Liu, H.; Xue, Q.; Li, X.; Chueh, C.-C.; Yip, H.-L.; Zhu, Z.; Jen, A. K. Highly Efficient All-Inorganic Perovskite Solar Cells with Suppressed Non-Radiative Recombination by a Lewis Base. *Nat. Commun.* **2020**, *11*, No. 1500477.
(58) Tan, H.; Che, F.; Wei, M.; Zhao, Y.; Saidaminov, M. I.; Todorović, P.; Broberg, D.; Walters, G.; Tan, F.; Zhuang, T. Dipolar Cations Confer Defect Tolerance in Wide-Bandgap Metal Halide Perovskites. *Nat. Commun.* **2018**, *9*, No. 3100.
(59) Kour, P.; Chenna Reddy, M.; Naphade, R.; Ogale, S. Quaternary Alkylammonium Salt Incorporated 2d/3d Mixed Halide Perovskite with Highly Enhanced Photoluminescence and Arrested Iodide/Bromide Phase Segregation. *APL Mater.* **2018**, *6*, No. 086107.
(60) Chen, W.; Chen, H.; Xu, G.; Xue, R.; Wang, S.; Li, Y.; Li, Y. Precise Control of Crystal Growth for Highly Efficient CsPbI2Br Perovskite Solar Cells. *Joule* **2019**, *3*, 191−204.

https://dx.doi.org/10.1021/acsaem.0c01520
ACS Appl. Energy Mater. 2020, 3, 11641−11654

(61) Wang, C.; Zhang, J.; Duan, J.; Gong, L.; Wu, J.; Jiang, L.; Zhou, C.; Xie, H.; Gao, Y.; He, H. All-Inorganic, Hole-Transporting-Layer-Free, Carbon-Based CsPbIBr2 Planar Perovskite Solar Cells by a Two-Step Temperature-Control Annealing Process. *Mater. Sci. Semicond. Process.* **2020**, *108*, No. 104870.
(62) Xiao, Y. Y.; Meng, Y.; Gao, H.; Chen, Y.; Meng, Q.; Bai, Y.; Wang, H.; Zhang, Y.; Yan, H.; Han, C. B. Flexible Perovskite Solar Cells Fabricated by a Gradient Heat Treatment Process. *Sustainable Energy Fuels* **2020**, *4*, No. 824.
(63) Ramsdell, L. S. Studies on Silicon Carbide. *Am. Mineral.* **1947**, *32*, 64−82.
(64) Gratia, P.; Zimmermann, I.; Schouwink, P.; Yum, J.-H.; Audinot, J.-N.; Sivula, K.; Wirtz, T.; Nazeeruddin, M. K. The Many Faces of Mixed Ion Perovskites: Unraveling and Understanding the Crystallization Process. *ACS Energy Lett.* **2017**, *2*, 2686−2693.
(65) Huang, L.; Hu, Z.; Xu, J.; Zhang, K.; Zhang, J.; Zhu, Y. Multi-Step Slow Annealing Perovskite Films for High Performance Planar Perovskite Solar Cells. *Sol. Energy Mater. Sol. Cells* **2015**, *141*, 377−382.
(66) Baikie, T.; Fang, Y.; Kadro, J. M.; Schreyer, M.; Wei, F.; Mhaisalkar, S. G.; Graetzel, M.; White, T. J. Synthesis and Crystal Chemistry of the Hybrid Perovskite (CH3NH3)PbI3 for Solid-State Sensitised Solar Cell Applications. *J. Mater. Chem. A* **2013**, *1*, 5628−5641.
(67) Heiderhoff, R.; Haeger, T.; Pourdavoud, N.; Hu, T.; Al-Khafaji, M.; Mayer, A.; Chen, Y.; Scheer, H.-C.; Riedl, T. Thermal Conductivity of Methylammonium Lead Halide Perovskite Single Crystals and Thin Films: A Comparative Study. *J. Phys. Chem. C* **2017**, *121*, 28306−28311.
(68) Tyson, T.; Gao, W.; Chen, Y.-S.; Ghose, S.; Yan, Y. Large Thermal Motion in Halide Perovskites. *Sci. Rep.* **2017**, *7*, No. 9401.
(69) Ohkura, Y.; Weisse, J. M.; Cai, L.; Zheng, X. Flash Ignition of Freestanding Porous Silicon Films: Effects of Film Thickness and Porosity. *Nano Lett.* **2013**, *13*, 5528−5533.
(70) Dharmadasa, R.; Dharmadasa, I.; Druffel, T. Intense Pulsed Light Sintering of Electrodeposited Cds Thin Films. *Adv. Eng. Mater.* **2014**, *16*, 1351−1361.
(71) Laidler, K. J. The Development of the Arrhenius Equation. *J. Chem. Educ.* **1984**, *61*, 494.

https://dx.doi.org/10.1021/acsaem.0c01520
ACS Appl. Energy Mater. 2020, 3, 11641−11654